ADVANCED MATERIALS
www.advmat.de

Ultra-Stiff yet Super-Elastic Graphene Aerogels by Topological Cellular Hierarchy

Yuxing Xia, Huasong Qin, Wenhao Tong, Yuxiang Qi, Kaiwen Li, Yingjun Liu, Zhen Xu, Yilun Liu, Kai Pang, Chao Gao,* and Weiwei Gao**

Lightweight cellular materials with high stiffness and excellent recoverability are critically important in structural engineering applications, but the intrinsic conflict between these two properties presents a significant challenge. Here, a topological cellular hierarchy is presented, designed to fabricate ultra-stiff (>10 MPa modulus) yet super-elastic (>90% recoverable strain) graphene aerogels. This topological cellular hierarchy, composed of massive corrugated pores and nanowalls, is designed to carry high loads through predominantly reversible buckling within the honeycomb framework. The compressive modulus of the as-prepared graphene aerogel is nearly twice that of conventional graphene aerogel. This high-stiff graphene aerogel also exhibits exceptional mechanical recoverability, achieving up to 60% strain recovery over 10 000 fatigue cycles without significant structural failure, outperforming most previously reported porous lattices and monoliths. It is further demonstrated that this graphene aerogel exhibits superior energy dissipation and anti-fatigue dynamic impact properties, with an energy absorption capacity nearly an order of magnitude greater than that of conventional aerogels. These exceptional properties of the topological cellular graphene aerogel open new avenues for high-energy bullet protection, offering great promise for the development of lightweight, armor-like protective materials in transportation and aerospace applications.

1. Introduction

Lightweight cellular materials (LCMs) feature high porosity and a high stiffness-to-weight ratio, making them suitable for a wide range of applications in structural engineering,[1–4] energy absorption,[5–7] thermal insulation,[8–11] and other functional areas.[12–20] High stiffness is a critical prerequisite for engineering performance, while elastic recoverability determines their structural reliability and long-term durability. However, these properties are generally mutually exclusive in LCMs.[21,22] This conflict arises primarily due to the strong correlation between stiffness and the thickness of cell walls in LCMs.[23] Thick walls in high-stiffness monoliths are prone to failure due to the dramatic increase in internal tension during deformation,[24–27] particularly in brittle components.[24] As a result, previous high-stiffness monoliths often experience catastrophic damage and poor structural tolerance under overload deformation.

The geometric design of structural cells has been a predominant strategy to improve the mechanical performance of lightweight materials.[28–30] In classical cellular materials, a small ratio of wall thickness to size is a characteristic feature that ensures structural recoverability under large deformation by enabling elastic buckling along the out-of-plane direction.[28,31] The arch-shaped lamellar structure has also been shown to exhibit superior elasticity by generating small arches during large deformation, which act as elastic buckling blocks.[32,33] However, these design concepts have typically been limited to low-density cellular materials, which do not satisfy the necessary high modulus required to bear loads in practical applications. Researchers have designed micro/nanolattices to fabricate high-stiffness LCMs by harnessing the architectural benefits of precisely controlling lattice topologies and assembling hierarchical structures from microscopic to macroscopic scales.[34,35] The octet-truss unit cell, a classical stretch-dominated structure, exhibits a superior stiffness-to-density ratio (specific strength) compared to other lightweight materials.[26,36] Nevertheless, this strategy compromises mechanical recoverability, with fractured strain typically below 20%.[37,38] To date, the conflict between high stiffness and structural recoverability has remained unresolved within the existing structural paradigm.

Y. Xia, Y. Qi, K. Li, Y. Liu, Z. Xu, K. Pang, C. Gao, W. Gao
MOE Key Laboratory of Macromolecular Synthesis and Functionalization
International Research Center for X Polymers
Department of Polymer Science and Engineering
Zhejiang University
38 Zheda Road, Hangzhou310027, China
E-mail: pangkai2015@zju.edu.cn; chaogao@zju.edu.cn; wwgao@zju.edu.cn

H. Qin, W. Tong, Y. Liu
Laboratory for Multiscale Mechanics and Medical Science, SV LAB
School of Aerospace
Xi'an Jiaotong University Institute
Xi'an 710049, P. R. China

Y. Liu, Z. Xu, C. Gao, W. Gao
Shanxi-Zheda Institute of Advanced Materials and Chemical Engineering
Taiyuan030032, China

C. Gao, W. Gao
Shaoxing Institute
Zhejiang University
2 Pingjiang Road, Shaoxin312099, China

The ORCID identification number(s) for the author(s) of this article can be found under https://doi.org/10.1002/adma.202417462

DOI: 10.1002/adma.202417462

Here, we resolve this conflict between high stiffness and superior elasticity by designing hierarchically topological cellular graphene aerogels (TCGAs). We employ 3D self-confined bubbling to transform thick cell walls into massive corrugated pores with nanowalls in honeycomb-structured graphene aerogels. The ultrathin nanowalls facilitate large elastic buckling deformations along the out-of-plane direction, thereby enhancing mechanical recoverability. Our experimental results and theoretical analysis demonstrate that the massive corrugated pores significantly improve loading-bearing capacity and mitigate stress concentration at the joints in the topological cells. This results in both high stiffness (12 MPa) and exceptional recoverability (90%) for TCGAs. Moreover, our high-stiffness aerogels maintain up to 60% recoverability after 10 000 fatigue cycles with no structural failure, surpassing the performance of previously reported carbon-based aerogels, monoliths, and micro/nanolattices. This highly stiff yet super-elastic TCGA contributes to superior energy dissipation, and fatigue impacts energy absorption performance. As proof of concept, the TCGA sandwich is applied in high-speed (≈200 m s^{-1}) ballistic impact protection, achieving extraordinary ballistic resistance performance.

2. Result and Discussion

2.1. Fabrication of Ultra-Stiff and Super-Elastic TCGAs

Figure 1A schematically illustrates the two-step method used to fabricate TCGAs. First, we employ the freezing-drying technique to fabricate a honeycomb-like graphene oxide (GO) framework, which consists of polyhedral cells and thick solid walls. Next, 3D self-confined bubbling is used to transform the solid walls into massive corrugated pores with nanowalls, leading to a hierarchically topological cellular structure. This self-confined effect results in coaxial expansion during bubble foaming within the 3D framework, as demonstrated by in-situ observation in a hexagonal cell model (Figure S1 and Movie S1, Supporting Information). Figure 1B–E reveals the multiscale structure of TCGAs from macroscopic to microscopic levels. The TCGA exhibits the typical honeycomb-like network with large pores from 100 to 200 µm, with cells typically exhibiting a polyhedral shape derived from ice crystal templates (Figure 1B). The thick walls of freeze-dried graphene aerogels (FDGAs) with a density of 90 mg cm^{-3} with a thickness of ≈1.2 µm (Figure S2C, Supporting Information) were deformed by bubbles to form numerous corrugated pores (2–20 µm) and ultrathin walls (Figure 1C–E). TEM analysis showed that the thickness of these ultrathin walls was reduced to ≈40 nm (Figure 1F), which is 30 times thinner than the original. Due to the 3D self-confined bubbling conducted within the honeycomb framework, the density of TCGA remained nearly the same as that of FDGAs, which was adjusted from 10 to 200 mg cm^{-3} (Figures S2 and S3, Supporting Information). The corrugated pores of TCGA with a density of 90 mg cm^{-3} were regulated by the foaming time, varying from ≈2 to ≈8 µm, showing a tendency to grow rapidly and then slowly (Figures S4 and S5, Supporting Information).

We further revealed that the TCGA exhibited high stiffness and superior recoverability. As shown in Figure 1F, the lightweight TCGA (≈1 g) can support 3000 times of its weight without significant deformation, indicating its high stiffness and mechanical integrity. The TCGA can rebound a steel ball (14 g, falling height of 80 cm) with a fast recovery speed of ≈2000 mm s^{-1} (Figure 1G), which is significantly faster than previously reported carbon-based aerogels.[31,32,39–43] Ashby plot of Young's modulus and recovery strain (Figure 1H) was used to compare the mechanical performance of our TCGAs at different densities (10–200 mg cm^{-3}) with previously reported carbon-based porous materials. Our TCGAs not only exhibited higher recoverable strain than low-density materials (graphene aerogels, CNT-based aerogels and so on) but also out-performed most high-density materials (carbon microlattices, pitch-based foams, and graphene monoliths) in terms of Young's modulus. These observations demonstrate that the topological cellular hierarchy design is an effective strategy for overcoming the engineering limitations of lightweight materials (Table S1, Supporting Information).[21,30,31,36,44–53]

2.2. Deformation Mechanism of the Topological Cellular Hierarchy

We performed finite element modeling (FEM) calculations to investigate the elastic deformation mechanism of ultrathin graphene walls (**Figure 2A**). The inner side of the cell walls was subjected to compressive deformation, while the outer side experienced tensile deformation during bending. We found that the maximum tensile strain of thick walls over 1 µm increased linearly with bending deflection, rapidly reaching the critical fracture strain of 3% (with only 2 µm deflection), indicating brittle deformation behavior.[54] Notably, the tensile strain of thinner walls with thickness below 1 µm exhibited a slow, non-linear increase with deflection, preventing the critical fracture strain from being exceeded. Thus, thinner walls were preferable for adopting flexural-dominated deformation with reversible buckling,[28] enabling the super-elasticity of TCGA (Figure S6, Supporting Information). We chose self-standing graphene films as a structural model to verify the critical of ultra-thin cell walls in recoverability through in situ compression (Figure 2B). The thin graphene film was easily recovered to its original shape without failure, indicating that the tensile strain during the entire bending process remained below the critical fracture strain. In contrast, the thicker film, which experienced large tensile strains during bending, exhibited significant permanent fracture behavior.[54] We also observed slippage of the graphene sheets in the thick films through sectional SEM analysis, indicating a pulled-out fracture due to tension during the bending process (Figure S7, Supporting Information). Furthermore, we investigated the strain–stress curves of graphene films during bending tests (Figure S8, Supporting Information). The thick film showed a sudden drop at a minimal strain (≈2%) due to interlayer fracture, while the thin film maintained a completely closed loop even under 80% strain. These observations further demonstrate that the ultrathin characteristic of the corrugated nanowalls is the intrinsic factor enabling the super-elasticity of TCGAs.

We conducted an in situ SEM inspection to study the microstructure evolution of GAs during compression at a maximum strain of 60%. For conventional FDGA, the permanent deformation was nearly 60% even during the first cycle, exhibiting typical brittle deformation behavior (Figure 2C). In SEM

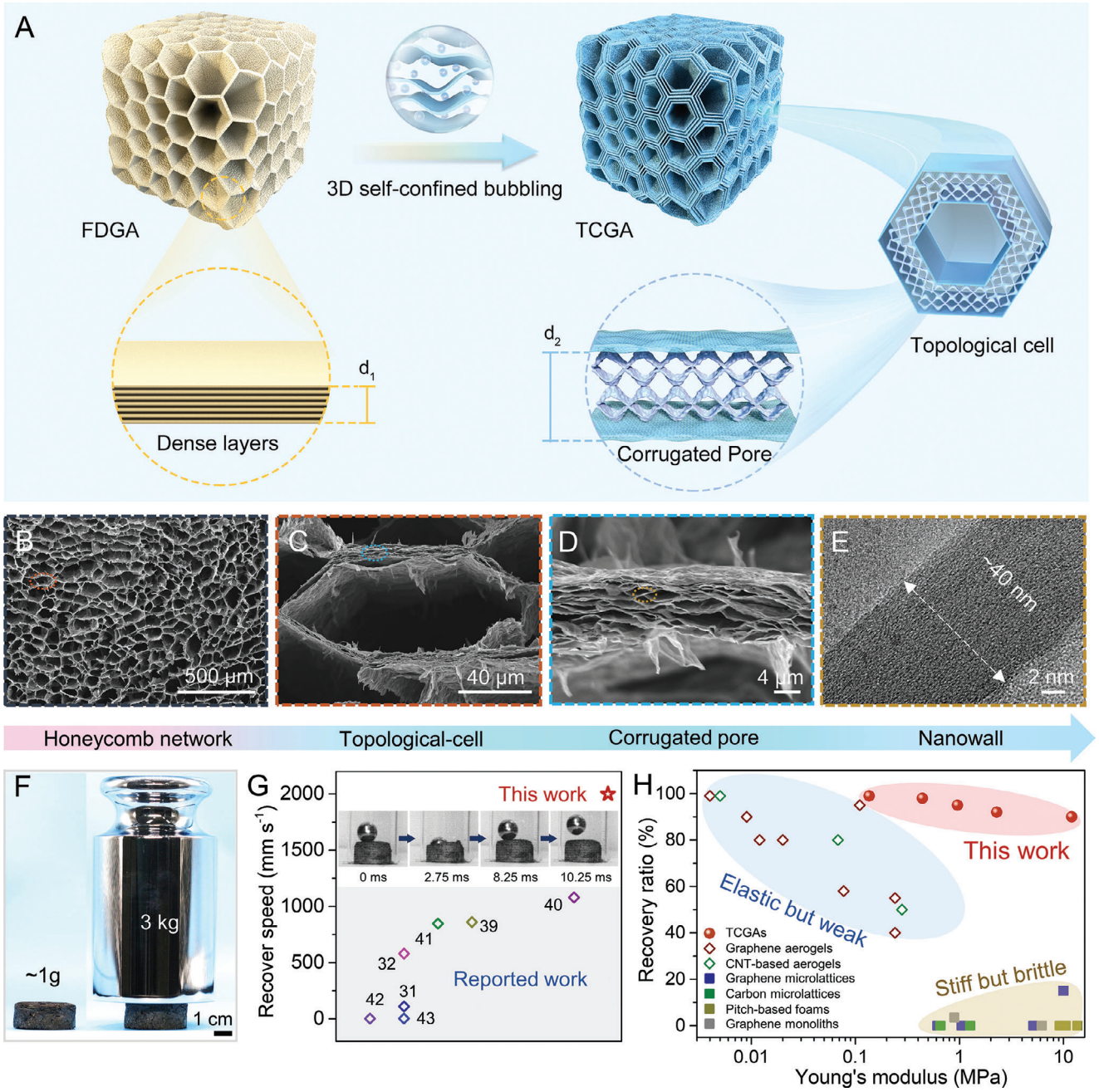

Figure 1. Fabrication of ultra-stiff and super-elastic graphene aerogels with a topological cellular hierarchy. A) Schematic illustration of the fabrication process for the topological cellular hierarchical structure by the 3D self-confined bubbling within the graphene honeycomb framework. B–E) SEM and HR-TEM images of the hierarchical structure of TCGA. F) The ultra-stiff TCGA can support up to ≈3000 times of its weight without deformation. G) Comparison of recovery speed between our aerogel and previously reported carbon-based aerogels. Insets are real-time images during a steel ball rebound test. H) Ashby plot of mechanical stiffness versus recovery ratio of TCGA and reported carbon-based porous materials.

magnifications, we observed many cracks in the thick walls and fragments of struts in the 3D network of FDGA during the compression process (Figure S9, Supporting Information). In comparison, the TCGA almost recovered to its original shape after compression without structural damage (Figure 2D), benefiting from the buckling elasticity of ultrathin walls. Even at 99% compressive strain, the corrugated nanowalls of TCGA generally tended to deform into several small curved structures instead of collapsing and could instantly spring back to their original shape after the load was released (Figure S10, Supporting Information). We found that many corrugated nanowalls in the (TCGA) served as load-bearing units rather than a thick wall in one basic block (FDGA), providing high stiffness at the initial deformation by mimicking a corrugated board at the microscale. The multistage fracture morphology of corrugated pores further demonstrated the higher energy dissipation efficiency of

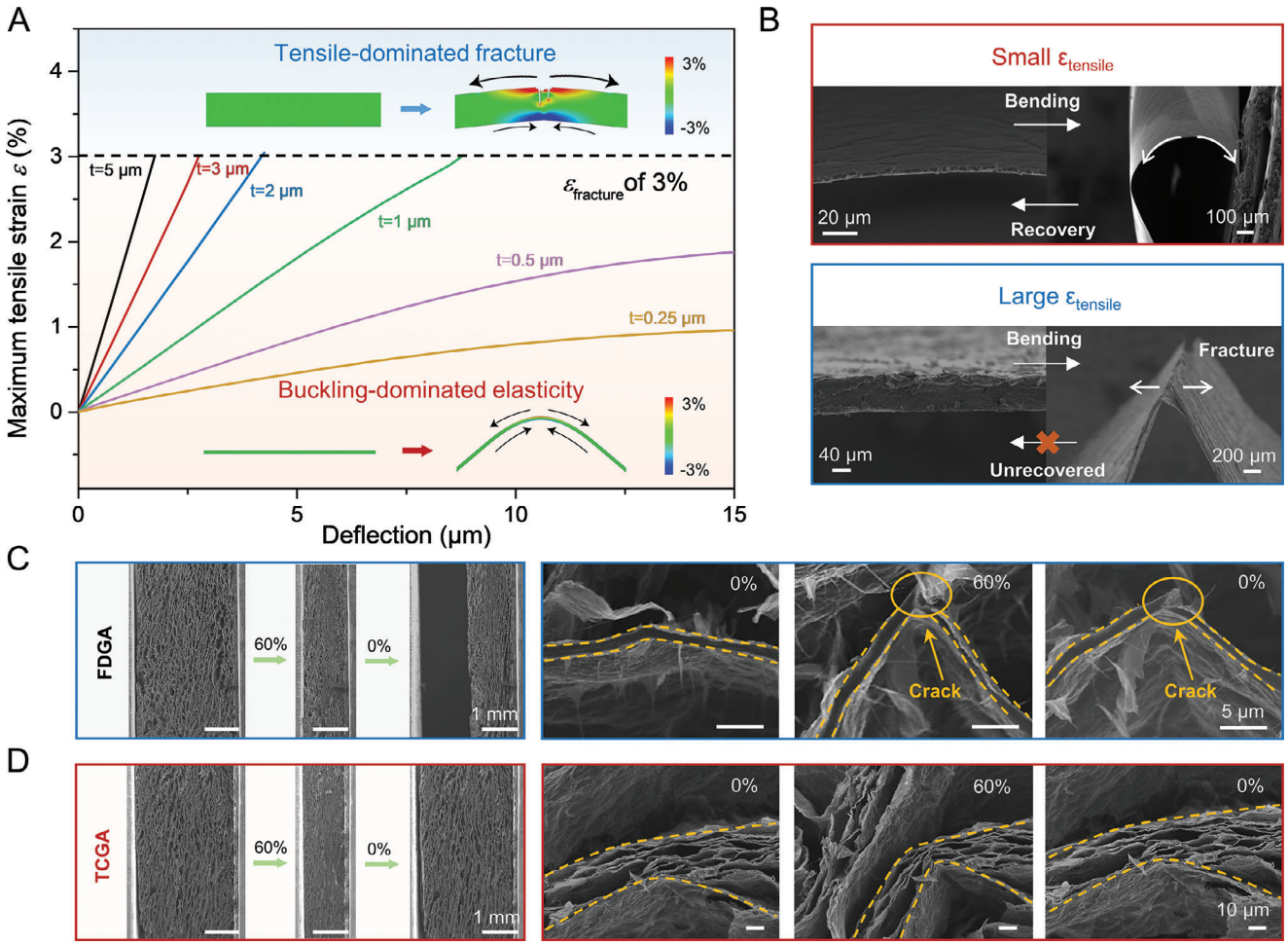

Figure 2. Elastic deformation mechanism of thin-wall cellular materials. A) Relationship between deflection and maximum tensile strain during bending deformation. B) In situ bending tests of thick and thin graphene films. C,D) In situ SEM images showing the structural changes of FDGA and TCGA during compress-release cycles.

TCGA compared to conventional FDGA (Figure S11, Supporting Information).

We extracted the single hexagonal graphene cell as a structural model to validate the mechanical superiority of corrugated pores. Classical and topological cells were the representative structures of FDGA and TCGA, respectively (**Figure 3**A). We demonstrated that the compressive force of the topological cell was ≈90 times and ≈3 times higher than that of the classical cell in the *XY*-plane and *XZ*-plane directions, respectively (Figure 3B,C). After loading was released (60% compressive strain), the topological cell completely recovered to its original height in both directions (Movie S2, Supporting Information). In contrast, the classical cell showed obvious fracture behavior at the structural joints, causing irreversible deformation after the loading release (Movie S3, Supporting Information). These results were consistent with the FEM analysis (Figure 3D; Figures S12 and S13, Supporting Information), confirming the mechanical superiority of the topological cellular hierarchy. Moreover, we revealed that the topological cell displayed a more uniform stress distribution than the classical cell (Figure 3E; Figure S14, Supporting Information), which suppressed joint fracture caused by stress concentration. Furthermore, we prepared a series of topological cells with different expansion ratios (*r*, the ratio of $r_{micro\text{-}pore}/r_{macro\text{-}cell}$, where $r_{micro\text{-}pore}$ is the thickness of the continuous corrugated pore network on the wall and $r_{macro\text{-}cell}$ is the radius of the framework hexagonal cell) (Figure 3F). The average size of the corrugated pores increased from ≈10 to ≈40 μm, with the expansion ratio ranging from 7% to 96%, accompanied by a shrinking of the radius of the inner coaxial hexagonal cell. As the expansion ratio exceeded ≈40%, the compressive force and mechanical recoverability of the topological cell were significantly enhanced (Figure 3G; Figure S15, Supporting Information). These results demonstrate that the corrugated nanowall hierarchy is an optimal structure to promote both the mechanical stiffness and elasticity of GAs simultaneously.

2.3. Mechanical Properties of TCGAs

Figure 4A shows the compression-release cycle of TCGA and FDGA with a density of 90 mg cm^{-3} under 60% strain. The compression strength and Young's modulus of TCGA exhibited ≈165% and ≈173% enhancements over that of FDGA at the same

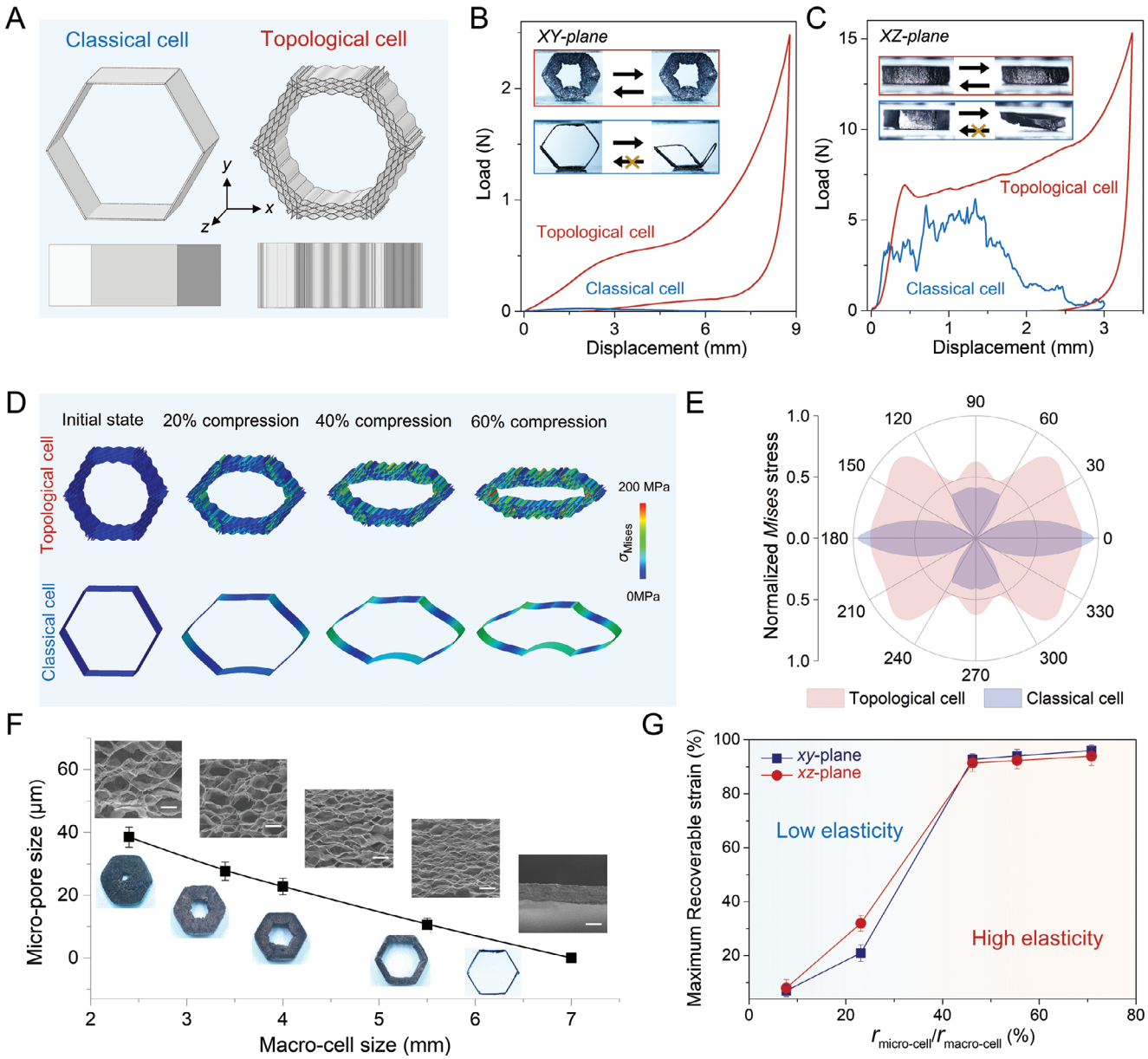

Figure 3. Mechanical behavior of a single topological cell. A) Finite element model of the classical cell and topological cell. Experimental compressive load displacement of the classical cell and topological cell along the B) *XY*-plane and C) *XZ*-plane under 60% compression strain. Insets show the morphologies of cells before and after compression. D) *Mises* stress profiles of cells with microstructure evolution during 60% compression. E) Normalized *Mises* stress distribution of the two cells at 60% compression, revealing the superior load-dissipation capability of the topological cell. F) Micro-pore size of the corrugated cell versus the macro-cell size of the inner coaxial hexagonal cell. Insets show corresponding optical morphologies and SEM images. Scale bar, 50 μm. G) Maximum elastic deformability of the topological cell versus $r_{micro\text{-}pore}/r_{macro\text{-}cell}$ along two geometric directions, where $r_{micro\text{-}pore}$ is the thickness of the continuous corrugated pores network on the wall and $r_{macro\text{-}cell}$ is the radius of the framework hexagonal cell.

density, respectively. The modulus of TCGAs was always higher than that of FDGAs at different densities from 10 to 200 mg cm^{-3}, reaching 12 MPa at high density (Figure 4B; Figure S16, Supporting Information). Moreover, the compressive modulus was found to scale with wall thickness (t) as $E \approx t^3$ for TCGA but as $E \approx t^1$ for FDGA (Figure S17A, Supporting Information), indicating the highly enhanced efficiency of the designed corrugated pores. We further investigated the dependence of the wall thickness (t) and density (ρ) for FDGAs and TCGAs to analyze the influence of wall thickness on their mechanical recoverability. The power exponent (n) of 2 for the relationship between t as ρ in FDGAs indicated the rapid rise of t as ρ increased, but only an n of 0.5 for TCGAs (Figure 4C). At a density of 200 mg cm^{-3}, the wall thickness of TCGA was ≈240 times lower than that of FDGA, providing a fundamental foundation for the recoverable deformation (Figure S18, Supporting Information). Insets of Figure 4C show the morphologies of graphene aerogels after compression at different densities for FDGA and TCGA. At lower densities, both

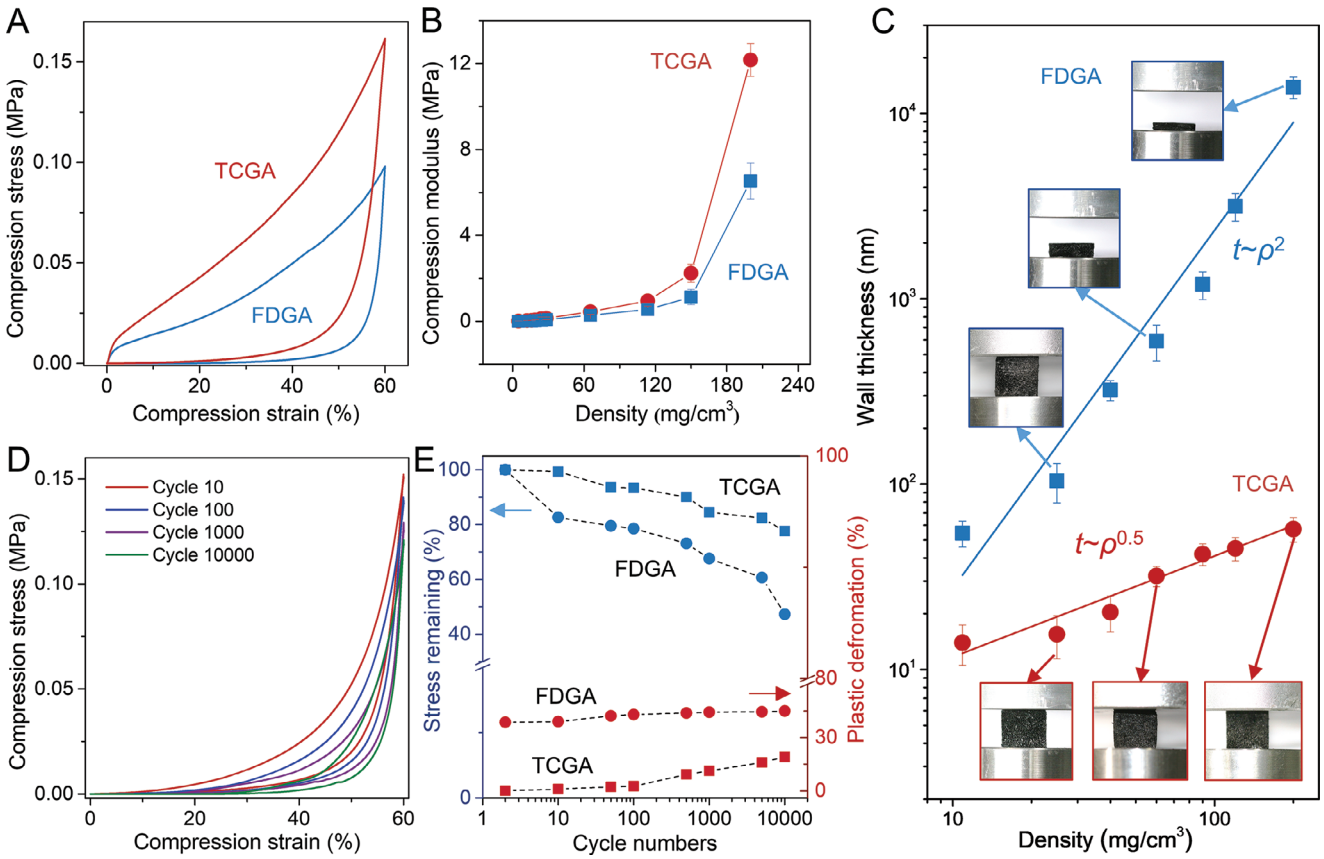

Figure 4. Mechanical properties of TCGAs. A) Compressive strain–stress curves of TCGA and FDGA at a density of 90 mg cm^{-3}. B) Comparison of Young's modulus of TCGA and FDGA at different densities. C) Wall thickness of TCGA and FDGA versus density. Insets show the morphologies of TCGA and FDGA with different wall thicknesses after 60% compressive strain. D) Stress–strain curves of TCGA at 60% strain for 10000 cycles. E) Stress remaining and plastic deformation of TCGA during 10 000 cycles at 60% strain.

types of GAs, with t below ≈100 nm, could display completely recoverable deformation to their original shapes. When the density increased to 60 mg cm^{-3}, the FDGA with t of 592 nm exhibited a reduction in recovery strain of ≈40% and even larger at higher densities, originating from the tensile-dominated brittle fracture of thick walls (Figure S17B, Supporting Information). The corrugated nanowall thickness of TCGAs was only ≈58 nm, even at the maximum density of 200 mg cm^{-3}, ensuring their excellent recoverability of ≈100% even at up to 90% strain.

The TCGA with corrugated nanowalls was further tested at different compress-release cycles to evaluate its fatigue resistance. We demonstrated that the TCGA exhibited high elasticity under uniaxial plane compression with a maximum strain of 90% (Figure S19, Supporting Information). At a density of 90 mg cm^{-3}, TCGA achieved a recoverable strain of up to 60% for 10 000 cycles with only 20% strain loss and 20% stress loss (Figure 4E), which has never been achieved in previously reported high-density monoliths. For conventional FDGA at the same density, it could only retain ≈40% of its initial compressive stress and experience up to ≈45% plastic deformation during a fatigue test of 10 000 cycles at 60% strain (Figure S20, Supporting Information). We also compared the fatigue performances of TCGA and FDGA at densities of 120 and 200 mg cm^{-3} (Figure S21, Supporting Information), further confirming the mechanical superiority of the corrugated nanowall structure. The plot of stress remaining versus maximum stress is shown in Figure S22 (Supporting Information), indicating that our TCGAs exhibited higher strength and larger stress retention than previously reported materials. These contrasts demonstrate that the corrugated nanowall design significantly enhances the efficiency of mechanical recoverability and anti-fatigue performance of aerogels.

2.4. Impact and Ballistic Resistance Performance of TCGAs

As proposed, the TCGA, featuring ultra-stiffness and superelasticity, is an ideal buffer material to absorb impact energy. We proposed a sandwiched structure using GAs and epoxy boards to evaluate the impact fatigue resistance performance through a drop hammer test system (**Figure 5A**). We compared the normalized energy absorption of pure epoxy boards, low-density GA (LDGA, soft but elastic), FDGA (stiff but brittle), and TCGA (ultra-stiff and super-elastic) sandwiches during the impact process by calculating the kinetic energy difference of the hammer (Figure 5B). We found that the impact energy absorption of the TCGA sandwich was ≈2.47 kJ m^{-1}, which is ≈4.2, ≈3.9, and ≈1.7 times higher than that of pure epoxy, LDGA, and FDGA

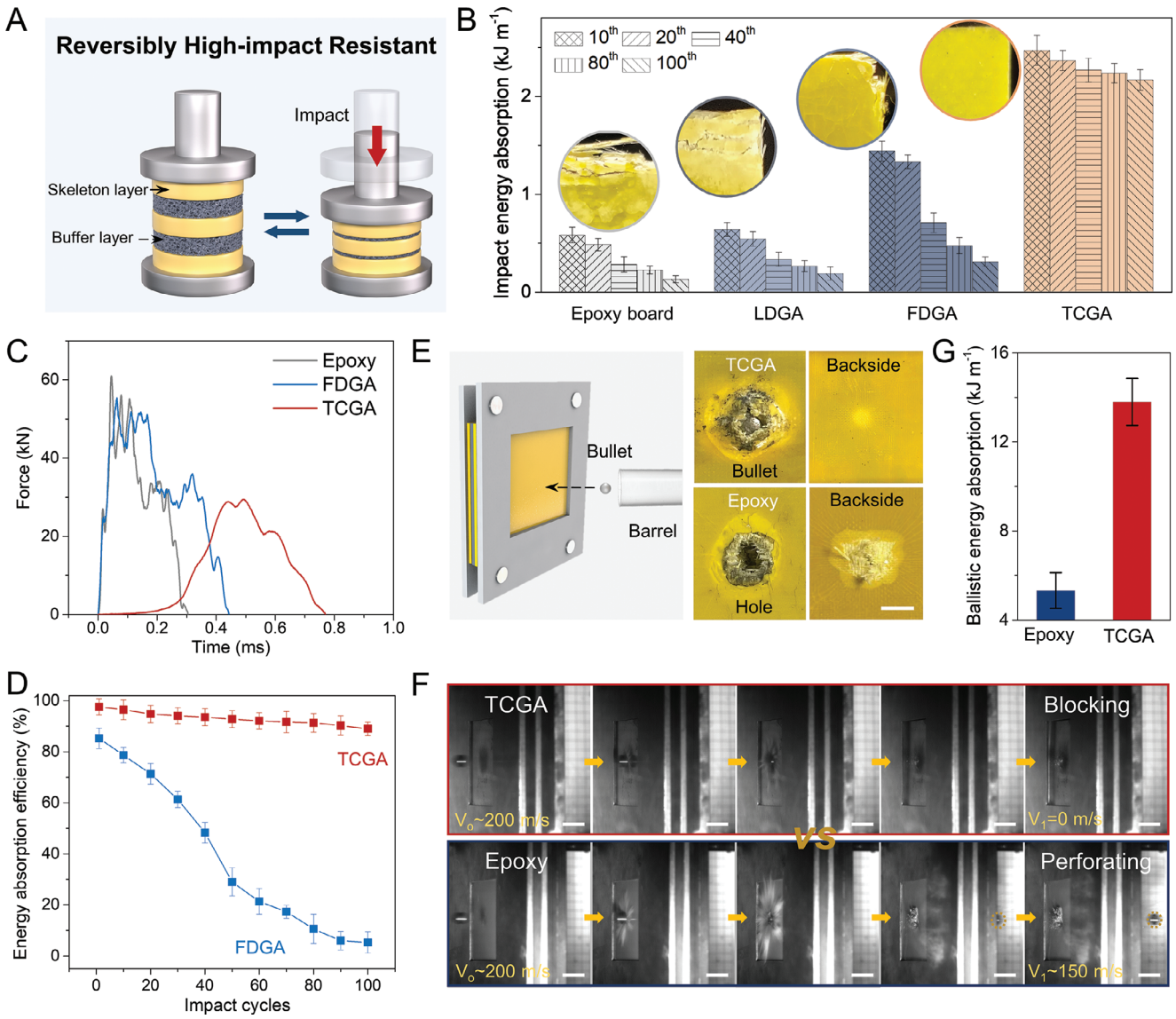

Figure 5. Impact and ballistic resistance performance of TCGAs. A) Design of the reversibly high-impact resistant structure. The epoxy board serves as the skeleton layer, and the GA functions as the buffer layer to absorb energy. B) Energy absorption variation of pure epoxy and different GA sandwiches during 100 impact cycles. Insets show surface morphologies after 100 cycles impact cycles. C) Impact force–time curves of pure epoxy and different GA sandwiches after 100 impact cycles. D) Energy absorption efficiency during 100 impact cycles, calculated by the $(v_{initial}^2 - v_{final}^2)/v_{initial}^2$. E) Illustration of the ballistic impact test. Photographs of the front and back sides of TCGA (top) and pure epoxy (bottom) after the bullet shock. Scale bar, 1 cm. F) High-speed snapshots of the ballistic impact process of the TCGA sandwich and epoxy. Scale bar, 20 mm. G) Ballistic energy absorption of the TCGA sandwich, showing nearly double the absorption of epoxy.

sandwiches, respectively. Additionally, the TCGA sandwich maintained a high and stable energy absorption ratio of ≈90% during repetitive impacts, always exhibiting an unchanged appearance even after 100 cycles. The maximum transient force of TCGA was only 31 kN, much lower than that of the pure epoxy and FDGA sandwiches (Figure 5C). After 100 impact cycles, the TCGA still significantly attenuated the impact forces and maintained a low peak force of 34 kN (Figure S23A, Supporting Information) due to its superior recoverability.[55–57] We further evaluated the energy absorption efficiency of TCGA and FDGA by calculating the ratio of $(v_{initial}^2 - v_{final}^2)$ to $v_{initial}^2$ (Figure 5D). The TCGA maintained a stable energy absorption efficiency of ≈90% during 100-cycle impacts, whereas the pure epoxy, LDGA, and FDGA sandwiches only retained an energy absorption efficiency of less than 5% after cycling (Figure S23B, Supporting Information).

We further assessed the potential application of the TCGA buffering sandwich through a ballistic impact test using an air-gun ballistic setup. The projectile, with a diameter of 12 mm, was shot through an air gun, striking the TCGA sandwich and pure epoxy at a velocity of ≈200 m s^{-1}, recorded by a high-speed camera (Figure 5E; Figure S24, Supporting Information). The ballistic absorption energy of the TCGA sandwich was ≈14 kJ m^{-1}, which is ≈2.6 times that of the epoxy boards (Figure 5F). Our

TCGA sandwich effectively blocked the high-speed projectile by absorbing the shock energy with large recoverable deformation (Figure 5G; Movie S4, Supporting Information). In contrast, the epoxy boards were easily penetrated by the projectile, which retained a high residual speed of ≈150 m s^{-1}. The dynamic high-impact resistance of TCGA expands the application value of lightweight aerogels toward engineering structural materials.

3. Conclusion

In summary, we present a topological cellular hierarchy of lightweight aerogels, realizing ultra-stiffness and super-elasticity. The buckling elasticity of nanowalls and the strengthening effect of corrugated pores are verified by experimental results and model validation. We reveal that the ultimate thickness of cell walls below 100 nm is the precondition for high recoverability. The as-prepared TCGA exhibited both a high stiffness of 12 MPa and exceptional recoverability of 90%, surpassing previously reported lightweight carbon-based porous materials. We further demonstrate that the TCGA can act as a high-efficiency buffer layer to resist over 100 repetitive impacts with a stable energy absorption efficiency of ≈90%. The TCGA also contributes to extraordinary ballistic resistance, blocking high-speed projectiles (200 m s^{-1}) and exhibiting great potential in engineering protective materials. This new topological cellular hierarchy provides the possibility to develop high-stiff and super-elastic structural aerogels, addressing practical demands in various applications.

4. Experimental Section

Fabrication of TCGAs: Aqueous GO dispersions were purchased from Hangzhou Gaoxi Technology Co. Ltd. (www.gaoxitech.com). GO aqueous dispersion with varying concentrations was placed in a refrigerator at −18 °C for 12 h, followed by freeze-drying for 24 h to fabricate GO aerogels with varying densities. The GO aerogels were then immersed in a N_2H_4/H_2O (30 wt.%) solution to initiate the 3D self-confined bubbling process. Finally, reduced graphene aerogels with a topological cellular structure and corrugated nanowalls (TCGA) were obtained by chemical reduction using a HI/HAc solution (volume ratio of 1:1). For comparison, the GO aerogels were directly reduced by HI/HAc vapor (volume ratio of 1:1) to produce chemically reduced graphene aerogels (FDGA).

Characterizations: The structure and morphology were examined using field-emission SEM (Hitachi S4800), HR-SEM (GeminiSEM 300), and TEM (FEI Titan G2 60–300). The rebounding experiment was recorded using a high-speed video camera (Phantom V611). Compressive tests were conducted on a microcomputer-controlled electronic universal testing machine (RGWT-4000-20, REGER) at a strain rate of 5 mm min^{-1}. Dynamic low-velocity impact tests were performed using a drop-weight impact testing system (Instron 9350). The ballistic test was conducted using an air gun setup, in which gas in the air cylinder was compressed at the release position, causing the projectiles to be instantaneously launched by the gas from the barrel. The ballistic energy absorption of the sample was defined as the kinetic energy loss of the projectile after impacting the sample, normalized by the sample thickness. High-speed digital cameras (20 000 frames per second) were used to capture the velocities of the projectile before and after it impacted the sample.

Finite Element Simulation and Analysis: The theoretical analysis of the superior elasticity of corrugated nanowalls and the geometric deformation and elastic behavior of the topological cell was conducted using finite element modeling (FEM)simulations. For the mechanical three-point bending tests of the corrugated nanowalls, self-standing graphene films with a length of 100 µm and thicknesses ranging from 0.25 to 5 µm were modeled to analyze the superior bending elasticity of high-stiffness aerogels. The Young's modulus and tensile strength of the graphene films were set to 2.3 GPa and 72 MPa, respectively, as measured by tensile testing (Figure S25, Supporting Information). The graphene films were assumed to be elastic, with brittle fracture criteria based on maximum strain employed to simulate failure behavior.

For the compression test of the classical cell, the geometric microstructure model was constructed as a regular hexagonal cell with a length (L) of 50.4 µm, height (H) of 43.7 µm, and wall thickness of 1.0 µm. For the compression test of the topological cell, the geometric microstructure was simplified to a multilayer porous hexagon with a wall thickness of 0.16 µm, ensuring the total mass of the classical and topological cell models remained constant. To counteract numerical instability phenomena, such as the hourglass effect, both models were meshed using fully integrated 4-node shell elements. In all simulations, compression was applied by a rigid plane with uniform displacement. For both models, the edges along the remaining axes were left unconstrained, free of traction or displacement. Additionally, the compressive velocity was maintained at 0.1 m s^{-1} for all models to ensure quasi-static loading conditions.

Supporting Information

Supporting Information is available from the Wiley Online Library or from the author.

Acknowledgements

Y.X. and H.Q. contributed equally to this work. This work was supported by the Natural Science Foundation of Zhejiang Province (No. LR24E030001), the National Natural Science Foundation of China (Nos. 52090030, 52090031 and 52272046), the National Key Research and Development Program of China (2022YFA1205300, 2022YFA1205301), "Pioneer" and "Leading Goose" R&D Program of Zhejiang (2023C01190), the Natural Science Foundation of Zhejiang Province (No. LR23E020003), Hundred Talents Program of Zhejiang University (188020*194231701/113, 112300+1944223R3/003 and 112300+1944223R3/004), the Fundamental Research Funds for the Central Universities (226-2023-00023, 226-2024-00074, 226-2024-00172 and 2023QZJH26), the Shanxi-Zheda Institute of New Materials and Chemical Engineering (Nos. 2022SZ-TD014, 2022SZ-TD011, 2022SZ-TD012), and the Joint Research Program of Shaoxing University and Shaoxin Institute, Zhejiang University (2023LHLG008).

Conflict of Interest

The authors declare no conflict of interest.

Data Availability Statement

The data that support the findings of this study are available from the corresponding author upon reasonable request.

Keywords

graphene aerogels, high stiffness, impact resistance, super-elasticity, topological hierarchy

Received: November 12, 2024
Revised: December 17, 2024
Published online:

[1] B. G. Compton, J. A. Lewis, *Adv. Mater.* **2014**, *26*, 5930.

[2] X. Yue, H. B. Yang, Z. M. Han, Y. X. Lu, C. H. Yin, X. Zhao, Z. X. Liu, Q. F. Guan, S. H. Yu, *Adv. Mater.* **2024**, *36*, 2306451.
[3] Z. H. Li, C. J. Chen, R. Y. Mi, W. T. Gan, J. Q. Dai, M. L. Jiao, H. Xie, Y. G. Yao, S. L. Xiao, L. B. Hu, *Adv. Mater.* **2020**, *32*, 1906308.
[4] Q. F. Guan, H. B. Yang, Z. M. Han, L. C. Zhou, Y. B. Zhu, Z. C. Ling, H. B. Jiang, P. F. Wang, T. Ma, H. A. Wu, S. H. Yu, *Sci. Adv.* **2020**, *6*, eaaz1114.
[5] A. du Plessis, S. M. J. Razavi, M. Benedetti, S. Murchio, M. Leary, M. Watson, D. Bhate, F. Berto, *Prog. Mater. Sci.* **2022**, *125*, 100918.
[6] S. H. Siddique, P. J. Hazell, H. X. Wang, J. P. Escobedo, A. A. H. Ameri, *Addit. Manuf.* **2022**, *58*, 103051.
[7] X. Y. Liang, G. D. Chen, I. M. Lei, P. Zhang, Z. Y. Wang, X. M. Chen, M. Z. Lu, J. J. Zhang, Z. B. Wang, T. L. Sun, Y. Lan, J. Liu, *Adv. Mater.* **2023**, *35*, 2207587.
[8] X. Zhao, Y. Liu, L. Zhao, A. Yazdkhasti, Y. Mao, A. P. Siciliano, J. Dai, S. Jing, H. Xie, Z. Li, S. He, B. C. Clifford, J. Li, G. S. Chen, E. Q. Wang, A. Desjarlais, D. Saloni, M. Yu, J. Kośny, J. Y. Zhu, A. Gong, L. Hu, *Nat. Sustain.* **2023**, *6*, 306.
[9] V. Apostolopoulou-Kalkavoura, P. Munier, L. Bergström, *Adv. Mater.* **2021**, *33*, 2001839.
[10] Z. M. Han, W. B. Sun, K. P. Yang, H. B. Yang, Z. X. Liu, D. H. Li, C. H. Yin, H. C. Liu, Y. X. Zhao, Z. C. Ling, Q. F. Guan, S. H. Yu, *Angew. Chem., Int. Ed.* **2023**, *62*, 202211099.
[11] S. Ahankari, P. Paliwal, A. Subhedar, H. Kargarzadeh, *ACS Nano* **2021**, *15*, 3849.
[12] Y. H. Li, C. K. Peng, H. M. Hu, S. Y. Chen, J. H. Choi, Y. G. Lin, J. M. Lee, *Nat. Commun.* **2022**, *13*, 1143.
[13] Y. M. Chen, L. Zhang, Y. Yang, B. Pang, W. H. Xu, G. G. Duan, S. H. Jiang, K. Zhang, *Adv. Mater.* **2021**, *33*, 2005569.
[14] C. Li, Y. W. Ding, B. C. Hu, Z. Y. Wu, H. L. Gao, H. W. Liang, J. F. Chen, S. H. Yu, *Adv. Mater.* **2020**, *32*, 1904331.
[15] B. Qin, Z. L. Yu, J. Huang, Y. F. Meng, R. Chen, Z. Chen, S. H. Yu, *Angew. Chem., Int. Ed.* **2023**, *62*, 202214809.
[16] H. F. Qin, Y. F. Zhang, J. G. Jiang, L. L. Wang, M. Y. Song, R. Bi, P. H. Zhu, F. Jiang, *Adv. Funct. Mater.* **2021**, *31*, 2106269.
[17] J. Garemark, X. Yang, X. Sheng, O. Cheung, L. C. Sun, L. A. Berglund, Y. Y. Li, *ACS Nano* **2020**, *14*, 7111.
[18] Y. D. Cui, J. H. Lin, Y. D. Zhai, C. Xu, C. J. Chen, C. Y. Chang, *Adv. Funct. Mater.* **2024**, *34*, 202401005.
[19] M. Zhou, D. Z. Chen, Q. Q. Chen, P. Chen, G. J. Song, C. Y. Chang, *Adv. Mater.* **2024**, *36*, 202312220.
[20] Z. H. Chen, Y. J. Hu, G. Shi, H. Zhuo, M. A. Ali, E. Jamroz, H. L. Zhang, L. X. Zhong, X. W. Peng, *Adv. Funct. Mater.* **2023**, *33*, 202214245.
[21] J. U. Surjadi, Y. S. Zhou, S. P. Huang, L. Q. Wang, M. Y. Li, S. F. Fan, X. C. Li, J. Z. Zhou, R. H. W. Lam, Z. K. Wang, Y. Lu, *Matter* **2022**, *5*, 4029.
[22] R. O. Ritchie, *Nat. Mater.* **2011**, *10*, 817.
[23] Y. M. Chen, R. Das, M. Battley, *Int. J. Solids. Struct.* **2015**, *52*, 150.
[24] L. R. Meza, S. Das, J. R. Greer, *Science* **2014**, *345*, 1322.
[25] J. Bauer, S. Hengsbach, I. Tesari, R. Schwaiger, O. Kraft, *Natl. Acad. Sci.* **2014**, *111*, 2453.
[26] X. Y. Zheng, H. Lee, T. H. Weisgraber, M. Shusteff, J. DeOtte, E. B. Duoss, J. D. Kuntz, M. M. Biener, Q. Ge, J. A. Jackson, S. O. Kucheyev, N. X. Fang, C. M. Spadaccini, *Science* **2014**, *344*, 1373.
[27] J. Yang, X. F. Li, S. Han, Y. T. Zhang, P. Min, N. Koratkar, Z. Z. Yu, *J. Mater. Chem. A.* **2016**, *4*, 18067.
[28] Y. J. Hu, Z. H. Chen, H. Zhuo, L. X. Zhong, X. W. Peng, R. C. Sun, *Adv. Funct. Mater.* **2019**, *29*, 1904472.
[29] M. Yang, N. F. Zhao, Y. Cui, W. W. Gao, Q. Zhao, C. Gao, H. Bai, T. Xie, *ACS Nano* **2017**, *11*, 6817.
[30] M. W. Peng, Z. Wen, L. J. Xie, J. Cheng, Z. Jia, D. L. Shi, H. J. Zeng, B. Zhao, Z. Q. Liang, T. Li, L. Jiang, *Adv. Mater.* **2019**, *31*, 1902930.
[31] L. Qiu, J. Z. Liu, S. L. Chang, Y. Wu, D. Li, *Nat. Commun.* **2012**, *3*, 1241.
[32] H. L. Gao, Y. B. Zhu, L. B. Mao, F. C. Wang, X. S. Luo, Y. Y. Liu, Y. Lu, Z. Pan, J. Ge, W. Shen, Y. R. Zheng, L. Xu, L. J. Wang, W. H. Xu, H. A. Wu, S. H. Yu, *Nat. Commun.* **2016**, *7*, 12920.
[33] H. L. Gao, Z. Y. Wang, C. Cui, J. Z. Bao, Y. B. Zhu, J. Xia, S. M. Wen, H. A. Wu, S. H. Yu, *Adv. Mater.* **2021**, *33*, 2102724.
[34] M. M. Wu, H. Y. Geng, Y. J. Hu, H. Y. Ma, C. Yang, H. W. Chen, Y. Y. Wen, H. H. Cheng, C. Li, F. Liu, L. Jiang, L. T. Qu, *Nat. Commun.* **2022**, *13*, 4561.
[35] T. A. Schaedler, A. J. Jacobsen, A. Torrents, A. E. Sorensen, J. Lian, J. R. Greer, L. Valdevit, W. B. Carter, *Science* **2011**, *334*, 962.
[36] R. M. Hensleigh, H. C. Cui, J. S. Oakdale, J. C. C. Ye, P. G. Campbell, E. B. Duoss, C. M. Spadaccini, X. Y. Zheng, M. A. Worsley, *Mater. Horiz.* **2018**, *5*, 1035.
[37] X. L. Yu, J. Zhou, H. Y. Liang, Z. Y. Jiang, L. L. Wu, *Prog. Mater. Sci.* **2018**, *94*, 114.
[38] A. Kudo, D. Misseroni, Y. C. Wei, F. Bosi, *Front. Mater.* **2019**, *6*, 169.
[39] Z. L. Yu, B. Qin, Z. Y. Ma, J. Huang, S. C. Li, H. Y. Zhao, H. Li, Y. B. Zhu, H. A. Wu, S. H. Yu, *Adv. Mater.* **2019**, *31*, 1900651.
[40] L. X. Lv, P. P. Zhang, T. Xu, L. T. Qu, *ACS. Appl. Mater. Inter.* **2017**, *9*, 22885.
[41] L. Zhuang, D. Lu, J. J. Zhang, P. F. Guo, L. Su, Y. B. Qin, P. Zhang, L. Xu, M. Niu, K. Peng, H. J. Wang, *Nat. Commun.* **2023**, *14*, 3178.
[42] J. Suhr, P. Victor, L. C. S. Sreekala, X. Zhang, O. Nalamasu, P. M. Ajayan, *Nat. Nanotechnol.* **2007**, *2*, 417.
[43] A. Y. Cao, P. L. Dickrell, W. G. Sawyer, M. N. Ghasemi-Nejhad, P. M. Ajayan, *Science* **2005**, *310*, 1307.
[44] Y. R. Li, J. Chen, L. Huang, C. Li, J. D. Hong, G. Q. Shi, *Adv. Mater.* **2014**, *26*, 4789.
[45] X. Xu, C. Guan, L. Xu, Y. H. Tan, D. W. Zhang, Y. Q. Wang, H. Zhang, D. J. Blackwood, J. Wang, M. Li, J. Ding, *ACS Nano* **2020**, *14*, 937.
[46] K. Pang, X. Song, Z. Xu, X. T. Liu, Y. J. Liu, L. Zhong, Y. X. Peng, J. X. Wang, J. Z. Zhou, F. X. Meng, J. Wang, C. Gao, *Sci. Adv.* **2020**, *6*, eabd4045.
[47] L. Qiu, B. Huang, Z. J. He, Y. Y. Wang, Z. M. Tian, J. Z. Liu, K. Wang, J. C. Song, T. R. Gengenbach, D. Li, *Adv. Mater.* **2017**, *29*, 1241.
[48] H. Y. Sun, Z. Xu, C. Gao, *Adv. Mater.* **2013**, *25*, 2554.
[49] X. C. Gui, J. Q. Wei, K. L. Wang, A. Y. Cao, H. W. Zhu, Y. Jia, Q. K. Shu, D. H. Wu, *Adv. Mater.* **2010**, *22*, 617.
[50] F. Wang, Y. Q. Jiang, Y. J. Liu, F. Guo, W. Z. Fang, Z. Xu, C. Gao, *Carbon* **2020**, *159*, 166.
[51] M. Ge, Z. M. Shen, W. D. Chi, H. Liu, *Carbon* **2007**, *45*, 141.
[52] X. T. Zhang, Z. Y. Sui, B. Xu, S. F. Yue, Y. J. Luo, W. C. Zhan, B. Liu, *J. Mater. Chem.* **2011**, *21*, 6494.
[53] Y. Lin, F. Liu, G. Casano, R. Bhavsar, I. A. Kinloch, B. Derby, *Adv. Mater.* **2016**, *28*, 7993.
[54] F. Guo, Y. Wang, Y. Q. Jiang, Z. S. Li, Z. Xu, X. L. Zhao, T. B. Guo, W. Jiang, C. Gao, *Adv. Mater.* **2021**, *33*, 2008116.
[55] J. P. Wu, Y. Wang, J. S. Zhang, C. Y. Zhao, Z. Y. Fan, Q. Shu, X. K. He, S. H. Xuan, X. L. Gong, *Matter* **2022**, *5*, 2265.
[56] S. M. Wen, S. M. Chen, W. T. Gao, Z. J. Zheng, J. Z. Bao, C. Cui, S. Liu, H. L. Gao, S. H. Yu, *Adv. Mater.* **2023**, *35*, 2211175.
[57] X. Zhang, K. J. Wu, Y. Ni, L. H. He, *Nat. Commun.* **2022**, *13*, 7719.